ACS Catalysis

pubs.acs.org/acscatalysis

Research Article

The Interplay between Hydroxyl Coverage and Reaction Selectivity of CO Conversion over the $MnOH_x$/Pt Catalyst

Rankun Zhang,[#] Le Lin,[#] Dongqing Wang, Yijing Liu, Yunjian Ling, Siqin Zhao, Rentao Mu,* and Qiang Fu*

Cite This: *ACS Catal.* 2022, 12, 11918−11926

Read Online

ACCESS | Metrics & More | Article Recommendations | Supporting Information

Downloaded via Rentao Mu on September 16, 2022 at 13:59:39 (UTC).
See https://pubs.acs.org/sharingguidelines for options on how to legitimately share published articles.

ABSTRACT: Hydroxyl groups (OH) and oxygen vacancies (V_O) have proven to be vital in numerous oxide catalytic systems for catalytic conversion of C1 molecules. In the present work, combining surface science experiments and density functional theory calculations, we construct a submonolayer $MnOH_x$ film on a Pt(111) substrate with different OH coverages (denoted as θ_{OH}) and reveal its impact on reaction pathways under ultrahigh vacuum (UHV) and a CO atmosphere. OH directly desorbs in the form of H_2O under UHV, while its evolution under a CO atmosphere can be divided into three stages with decreasing θ_{OH}: (i) $CO + 2OH \rightarrow CO_2 + H_2O$ ($85\% \leq \theta_{OH} \leq 94\%$); (ii) $CO + 2OH \rightarrow CO_2 + H_2 + O_L$ (O_L, lattice O; $50\% \leq \theta_{OH} \leq 85\%$); and (iii) $2CO + 2OH \rightarrow 2CO_2 + H_2$ ($26\% \leq \theta_{OH} \leq 50\%$). In nature, surface OH and CO can form carboxyl intermediates, which promote the H_2O generation and the O−H to Mn−H diffusion compared to the processes without CO assistance. Furthermore, as θ_{OH} decreases and V_O increases, H binding on $MnOH_x$/Pt(111) is weakened while OH binding is strengthened, which favors the generation of H_2 instead of H_2O. These results provide inspiration to understand the mechanism for H- or OH-involved CO conversion reactions and to modulate a reaction selectivity via tailoring OH and V_O densities.

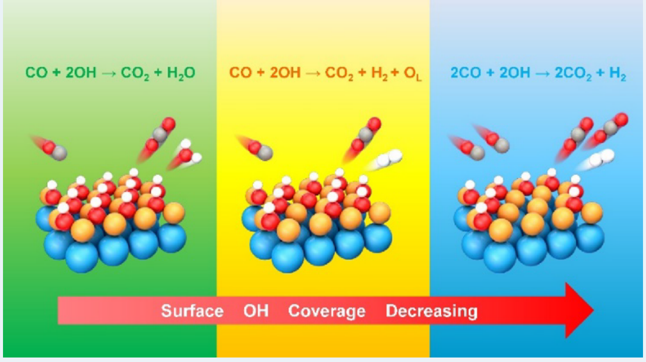

KEYWORDS: *hydroxyl, oxygen vacancy, CO conversion, reaction selectivity, interfacial catalysis*

INTRODUCTION

Clean H_2 production is important for many industrial applications, including methanol synthesis,[1−3] ammonia synthesis,[4,5] and proton exchange membrane fuel cells.[6−8] The water gas shift (WGS) reaction and CO preferential oxidation (PROX) reaction are thought to be potential pathways to produce H_2 and reduce CO content in H_2, respectively.[9−14] Extensive efforts have been made for understanding the mechanism of reaction between CO and surface OH, which is important for H_2 production and purification, mainly including confirmation of active sites, formation of intermediate species, and function of surface OH. In the WGS reaction, the associative mechanism and redox mechanism have been proposed to explain how the reaction proceeds.[15−18] In the associative mechanism, it is thought that CO directly reacts with surface OH to form intermediate species such as carboxyl and formate, which would decompose to produce H_2 and CO_2 afterward. In the redox mechanism, it is considered that surface OH does not interact with CO directly. Surface OH decomposes to produce active oxygen species (O*) and active hydrogen species (H*), then H_2 is formed by the combination of two H*, and CO reacts with O* to produce CO_2. However, the reaction mechanism of the WGS reaction is uncertain even in similar systems. For example, it has been reported that the Au/CeO_2 system[19] and Pt/CeO_2 system[20] follow the associative mechanism and the redox mechanism, respectively. In the PROX reaction, it is proposed that surface OH can react with CO to form intermediate species, which decomposes into CO_2 with a lower energy barrier.[12,21,22] The crucial step in these reactions is how surface OH reacts with CO, which is related to the OH type and coverage on the catalyst surface.

It has been reported that the type of surface OH affects the reaction activity.[19,20,23,24] Ribeiro et al.[23] studied the effect of the OH type in the Pt/MnO_x catalyst on WGS reactivity by in situ diffuse reflectance infrared Fourier transform spectroscopy, which shows that the bridging OH is the active one. In water-catalyzed CO oxidation, Nie et al.[24] reported that H_2O dissociates at the V_O site to produce OH on the Ce-top site and lattice hydroxyl ($O_{lattice}H$), and CO prefers to react with OH on the Ce-top site according to density functional theory (DFT) calculations. In addition, surface θ_{OH} has an effect on

Received: July 11, 2022
Revised: August 21, 2022

ACS Publications

© XXXX American Chemical Society

https://doi.org/10.1021/acscatal.2c03337
ACS Catal. 2022, 12, 11918−11926

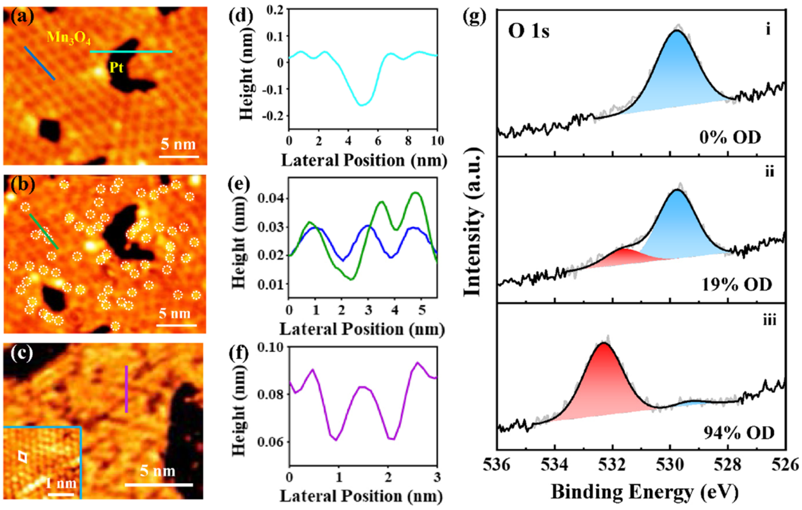

Figure 1. Controlling the hydroxylation degree of 0.85 ML Mn_3O_4/Pt(111). Same-area STM images of the Mn_3O_4/Pt(111) surface (a) before and (b) after exposure to 90 L D_2 at room temperature. Scanning parameters: (a) I_t = 0.1 nA, V_s = 2.0 V; (b) I_t = 0.2 nA, V_s = 2.0 V. (c) STM image of the Mn_3O_4/Pt(111) surface after exposure to 450 L D_2 at room temperature. Scanning parameters: I_t = 0.09 nA, V_s = 1.4 V. Inset: atomic-resolution STM image of the Mn_3O_4/Pt(111) surface after exposure to 450 L D_2 at room temperature. Scanning parameters: I_t = 0.09 nA, V_s = 0.2 V. (d) Line profile along the cyan line in panel (a). (e) Line profiles along the blue and green lines in panels (a) and (b), respectively. (f) Line profile along the purple line in panel (c). (g) XPS O 1s spectra of the Mn_3O_4/Pt(111) surface after exposure to different amounts of D_2 at room temperature, (i) 0 L, (ii) 90 L, and (iii) 300 L.

H_2 production in heterogeneous catalysis.[25,26] It has been found that the ultrahigh vacuum (UHV) desorption product of surface OH of the hydroxylated FeO film transforms from H_2O to H_2 with the decrement of surface θ_{OH} and the increment of V_O density.[25] Similar desorption behavior also happens on a hydroxylated CeO_2 film.[26] However, the influence of θ_{OH} on the CO conversion reaction and H_2 production is rarely studied.

Because of the difficulty in quantifying surface θ_{OH} of powder catalysts, a model monolayer $MnOH_x$ film (θ_{OH} = 94%) is constructed to investigate the influence of θ_{OH} of a metal oxide surface on H_2 production. Through surface science technologies, including X-ray photoelectron spectroscopy (XPS) and scanning tunneling microscopy (STM), and DFT calculations, it is found that the desorption product of OH is mainly H_2O when annealing the $MnOH_x$ film under UHV. While annealing the $MnOH_x$ film in CO, the reaction process is divided into three stages as θ_{OH} decreases and V_O density increases. First, CO reacts with interfacial OH to produce CO_2 and H_2O with a lower energy barrier than annealing under UHV in terms of H_2O generation. Second, reaction products turn to CO_2, lattice oxygen (O_L), and H_2 because of the weakened H binding and enhanced OH binding on Mn sites. Third, CO reacts with O_L to produce CO_2 apart from the reaction occurring in the second stage. It is also noteworthy that the $MnOH_x$ film reacts with CO more easily than the Mn_3O_4 film.

■ RESULTS AND DISCUSSION

Hydroxylation of Mn_3O_4/Pt(111). Figure 1a shows the STM image of MnO_x prepared by evaporating Mn in 1×10^{-7} mbar O_2 at 423 K, in which the nominal coverage is controlled at 0.85 monolayer (ML). The darker contrast region is a bare Pt(111) substrate, and the brighter contrast region represents the MnO_x film, which displays a grid-like structure. To ascertain this grid-like MnO_x, submonolayer MnO/Pt(111) was prepared as a reference and characterized by STM and XPS. Figure S1a shows the STM image of the MnO overlayer with a uniaxial row structure, which has been reported by Hagendorf et al.[27] The XPS O 1s (Figure S1b) peak located at 529.9 eV is assigned to O_L of MnO. Figure S1c shows that Mn $2p_{3/2}$ and $2p_{1/2}$ peaks are located at 640.9 and 652.3 eV, respectively. The satellite peaks of Mn $2p_{3/2}$ and $2p_{1/2}$ are located at 647.7 and 658.8 eV, respectively, and the distance between Mn $2p_{1/2}$ and its satellite peak is 6.5 eV. All are characteristic of MnO.[28,29] The XPS O/Mn ratio of MnO is normalized to 1.00. XPS measurement (Figure S2a) shows that the O 1s peak of MnO_x with a grid structure is located at 529.7 eV, which is assigned to O_L.[30] Figure S2b shows that Mn $2p_{3/2}$ and $2p_{1/2}$ peaks are located at 641.1 and 652.5 eV, respectively. Compared with MnO, the satellite peak of Mn $2p_{3/2}$ of MnO_x with a grid-like structure is invisible because of the overlapping with the Mn $2p_{1/2}$ peak, which is the feature of Mn_3O_4 species.[31] Using the XPS O/Mn ratio of MnO as a reference, that of MnO_x with a grid-like structure is determined to be 1.31. Therefore, it can be concluded that MnO_x with the grid structure is Mn_3O_4 species. Figure 1d suggests that the apparent height of the Mn_3O_4 film is determined to be ~1.87 Å. The XPS O 1s spectrum (Figure 1g(i)) suggests that oxygen species of the Mn_3O_4 film is O_L before exposure to D_2. The utilization of D_2 is for excluding the disturbance of background H_2 and H_2O.

Figure 1b shows the STM image of the same area with Figure 1a after exposure to 90 L D_2 at room temperature. Compared with Figure 1a, it can be seen that some bright spots emerge along the grid line in Figure 1b, which are marked by white dashed circles. Figure 1e shows that the apparent height of the Mn_3O_4 grid line increases by ~0.1 Å after exposure to 90 L D_2 at room temperature, indicating hydroxylation of the Mn_3O_4 film. In addition, the majority of bright spots are distributed on the Mn_3O_4 film adjacent to the bare Pt(111) substrate, which suggests the splitting of D_2 at the bare Pt substrate and the spillover of atomic deuterium from the bare Pt substrate to Mn_3O_4 film at room temperature. The XPS O

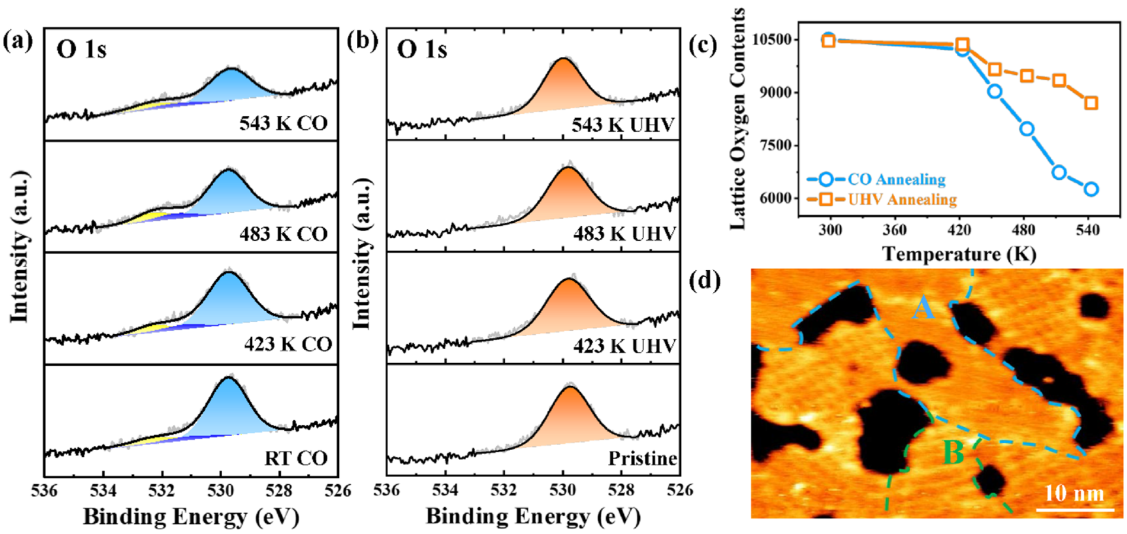

Figure 2. Transformation of 0.85 ML Mn_3O_4/Pt(111) under UHV and CO atmosphere. XPS O 1s spectra of the Mn_3O_4/Pt(111) surface annealing in (a) 5×10^{-7} mbar CO and (b) UHV from room temperature to 543 K. (c) XPS O_L contents of the Mn_3O_4/Pt(111) surface annealing in 5×10^{-7} mbar CO and UHV from room temperature to 543 K. (d) STM image of the Mn_3O_4/Pt(111) surface after annealing to 543 K in 5×10^{-7} mbar CO. Scanning parameters: I_t = 0.1 nA and V_s = 1.5 V.

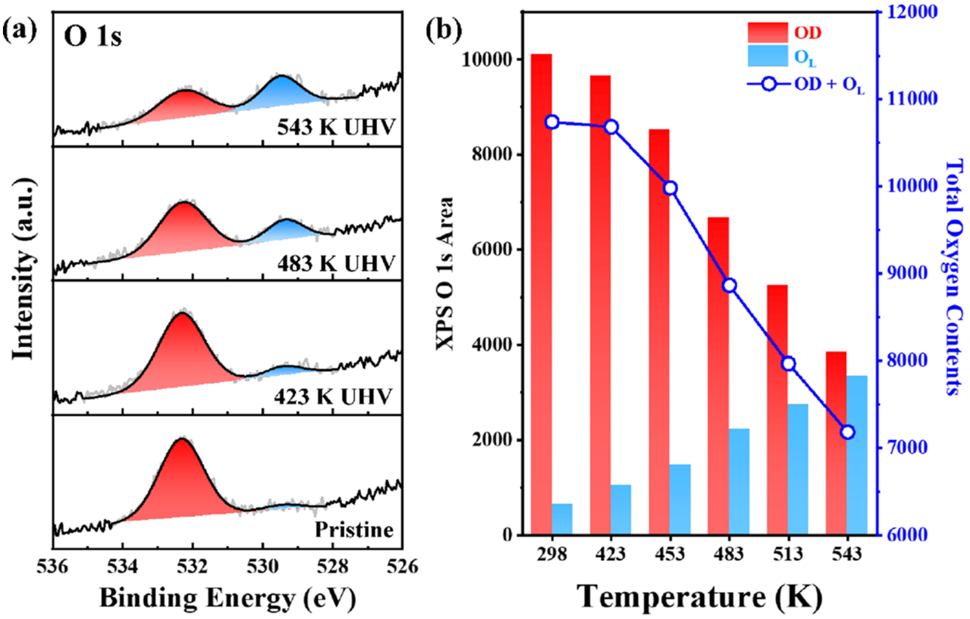

Figure 3. Desorption of surface OD of $MnOD_x$/Pt(111) under UHV. XPS (a) O 1s spectra (b) OD and O_L peak area and total oxygen contents of $MnOD_x$/Pt(111) annealing under UHV from room temperature to 543 K.

1s spectrum can be deconvoluted by two peaks, which are located at 529.7 and 531.6 eV, respectively (Figure 1g(ii)). The O 1s peak located at 531.6 eV is assigned to the OD group,[32] and the content of OD is 19%. After exposure to 450 L D_2 at room temperature, the STM image (Figure 1c) shows that the grid structure of the Mn_3O_4 film disappears and a triangular pattern emerges, indicating the structural transformation during the hydroxylation process. The inset of Figure 1c shows that the hydroxylated film exhibits a hexagonal structure. Figure 1f shows that the apparent height of the triangular pattern is determined to be ~0.23 Å. The triangular pattern is similar to the V_O dislocation loop on the hydroxylated FeO(111) film, which is formed by exposure to atomic hydrogen at room temperature and then flashing to 450 K in UHV.[33,34] The formation of the V_O dislocation loop is probably due to the lattice mismatch during the structural transformation process. Figure 1g(iii) shows that OD and O_L contents are 94 and 6%, respectively. Thus, an $MnOD_x$ film (θ_{OD} = 94%) can be obtained from the Mn_3O_4 film by dosing D_2 at room temperature.

Annealing Mn_3O_4/Pt(111) in the CO Atmosphere and UHV. For comparison with the $MnOD_x$ film, the initial Mn_3O_4 film under UHV and CO atmosphere was first investigated. Figure 2a,b shows XPS O 1s spectra of Mn_3O_4/Pt(111) annealed in 5×10^{-7} mbar CO and UHV to different temperatures, respectively. O 1s peaks located at 531.4 and 532.3 eV are assigned to CO adsorbed on bridging and on-top sites of the bare Pt(111) substrate, respectively.[35] Figure 2c displays O_L content of the Mn_3O_4 film after annealing in CO and UHV to different temperatures. O_L content of the Mn_3O_4

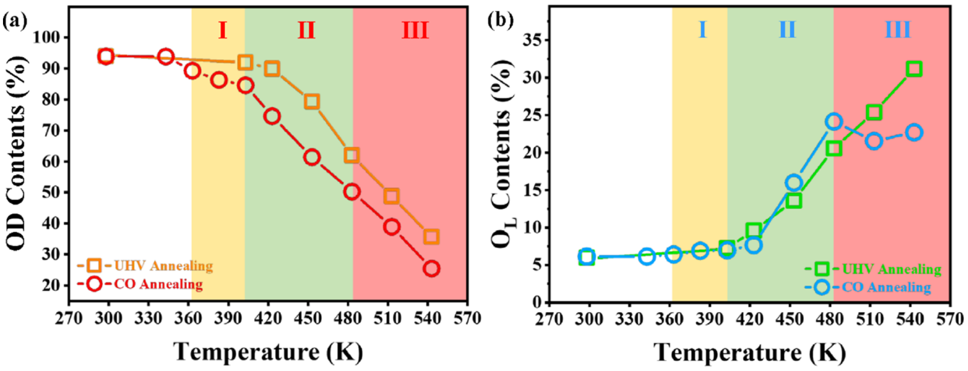

Figure 4. Three stages of reaction between surface OD of $MnOD_x$/Pt(111) and CO. XPS-derived (a) OD and (b) O_L contents of $MnOD_x$/Pt(111) annealing in 5×10^{-7} mbar CO and UHV from room temperature to 543 K. The main reaction upon annealing $MnOD_x$/Pt(111) in CO is proposed to be: (I) $CO + 2OD \rightarrow CO_2 + D_2O$ (363∼403 K); (II) $CO + 2OD \rightarrow CO_2 + D_2 + O_L$ (403∼483 K); (III) $CO + 2OD \rightarrow CO_2 + D_2 + O_L$ and $CO + O_L \rightarrow CO_2$ (483∼543 K).

film remains almost unchanged after annealing to 423 K in both CO and UHV. After annealing to 453 K in CO, O_L content of the Mn_3O_4 film decreases by 14%, and that decreases by 8% after annealing in UHV to 453 K. O_L content of the Mn_3O_4 film decreases to 60 and 83% after annealing to 543 K in CO and UHV, respectively. As expected, more O_L of Mn_3O_4 is consumed by annealing in CO than that in UHV when annealing from room temperature to 543 K. The reaction can be inferred to be:

$$CO + O_L \rightarrow CO_2 \tag{1}$$

Figure 2d displays the STM image of the Mn_3O_4 film after annealing to 543 K in CO. It can be observed that the MnO_x film is still flat after CO annealing. However, the change of the surface structure is obvious compared with the pristine Mn_3O_4 film shown in Figure 1a. In region A (marked by a blue dashed line), the uniaxial row structure indicates a characteristic MnO phase.[27] The grid structure is incomplete in region B (marked by a green dashed line), which can be seen as a transition structure from Mn_3O_4 to MnO. In the other regions, the grid structure can still be distinguished clearly. XPS Mn 2p and O 1s spectra are shown in Figure S3, and the O/Mn ratio is determined to be 1.07. Therefore, it can be concluded that CO reacts with O_L of the Mn_3O_4 film, and the Mn_3O_4 film with a grid structure is gradually reduced to MnO with a row structure during the annealing process.

Annealing $MnOD_x$/Pt(111) under UHV. Figure 3a,b presents XPS O 1s spectra and oxygen species content of $MnOD_x$/Pt(111) upon annealing under UHV to different temperatures. After annealing to 423 K under UHV, O 1s peak areas of OD and O_L remain almost unchanged. With the increment of annealing temperatures in UHV, the O 1s peak area of OD keeps on decreasing, whereas that of O_L keeps on increasing. After annealing to 543 K under UHV, OD content decreases by 58% and O_L content increases by 25%. The extent of OD content decrement is approximately two times compared with that of O_L content increment. This is consistent with the desorption process of surface OD in the form of D_2O, where the decrement of OD is two times than the increment of O_L:

$$2OD \rightarrow D_2O + O_L \tag{2}$$

Therefore, it can be concluded that the main desorption product of OH is H_2O when annealing the $MnOH_x$ film under UHV.

Annealing $MnOD_x$/Pt(111) in CO. STM was first applied to investigate the structural change when annealing $MnOD_x$ in the CO atmosphere. STM images of $MnOD_x$/Pt(111) before and after annealing to 438 and 498 K directly in CO are displayed in Figure S4. It is shown that the area of a brighter contrast region which represents surface OD of the Mn_3O_4 film decreases as the annealing temperature increases, indicating the consumption of OD by CO. In addition, there is a more darker contrast region around the bare Pt(111) substrate, which implies that the reaction starts from the interface between the $MnOD_x$ film and bare Pt(111) substrate. Figure 4a,b presents OD and O_L contents of $MnOD_x$/Pt(111) annealing in 5×10^{-7} mbar CO and UHV from room temperature to 543 K, respectively. Corresponding XPS O 1s spectra of $MnOD_x$/Pt(111) annealing in 5×10^{-7} mbar CO are shown in Figure S5. Compared with the Mn_3O_4 film, it is evident that the initial reaction temperature is lower on the $MnOD_x$ film (363 K) than that on the Mn_3O_4 film (423 K) when annealing in CO. The consumption of total oxygen species of the $MnOD_x$ film (52%) is more than that of the Mn_3O_4 film (40%) after annealing to 543 K in CO. The result indicates that the hydroxylated surface is more reactive with CO than the O_L surface.

More specifically, the reaction process can be divided into three stages when annealing the $MnOD_x$ film in CO from room temperature to 543 K. After annealing to 343 K in CO, O 1s peak areas of OD and O_L remain unchanged, suggesting that neither CO reacts with surface oxygen species nor OD desorbs at this temperature. After annealing to 363 K in CO, OD content decreases from 94 to 89% and O_L content remains unchanged, indicating that CO starts to react with OD of $MnOD_x$. OD content decreases to 85% and O_L content remains stable after annealing to 403 K in CO. Based on these results, the main reaction between CO and OD from 363 to 403 K should be:

$$CO + 2OD \rightarrow CO_2 + D_2O \ (85\% \leq OD \leq 94\%) \tag{3}$$

After annealing to 423 K in CO, OD content decreases from 85 to 75%, and O_L content increases from 6 to 8%. As the annealing temperature increases, more O_L species is produced. After annealing to 483 K in CO, OD content decreases by 34%, and O_L content increases by 17%. The degree of OD content decrement is approximately two times that of O_L content increment, which is similar to reaction 2. Nevertheless, the possibility that the decrement of OD is not associated with

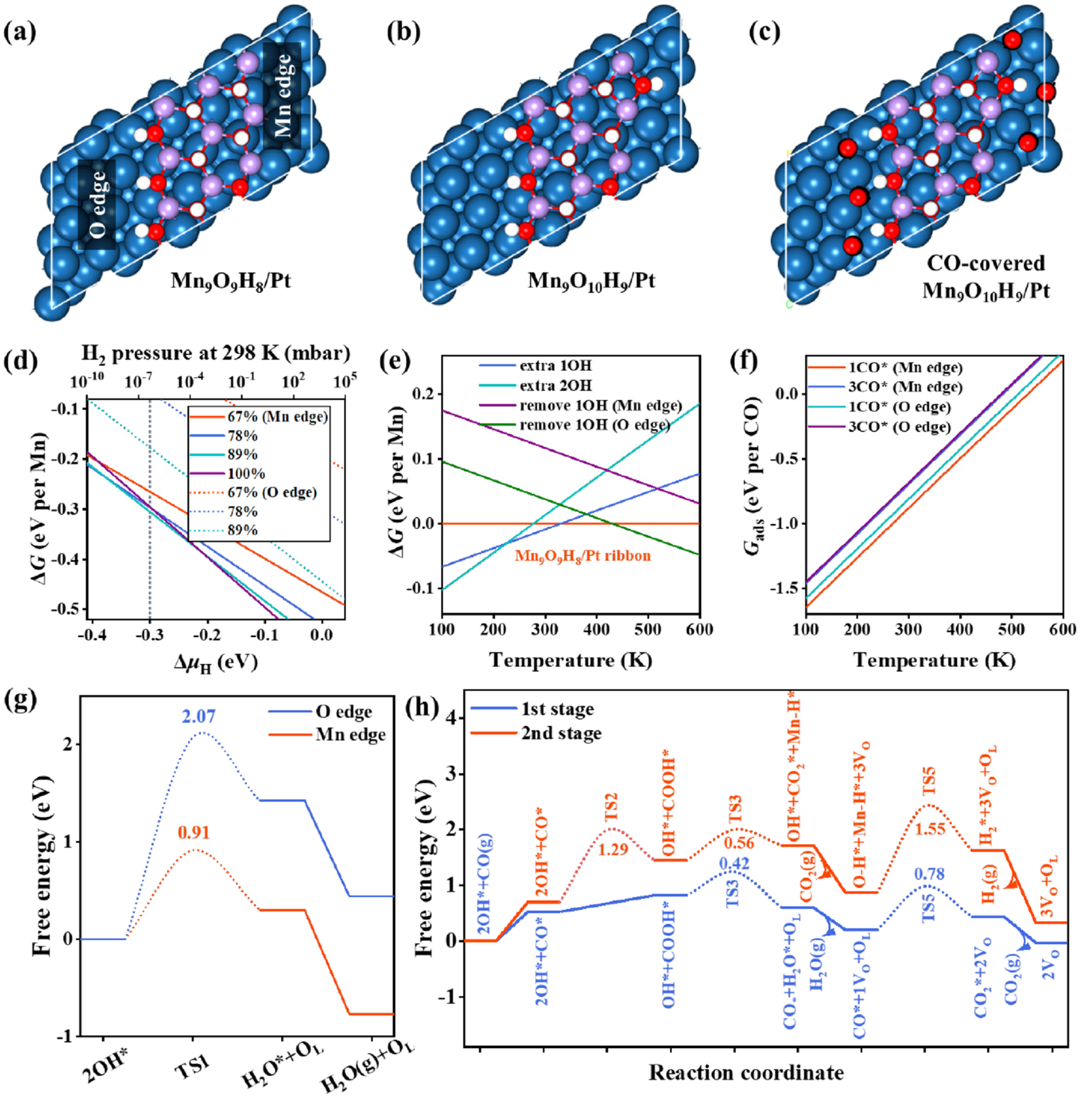

Figure 5. DFT insights into H_2O and H_2 generations over $MnOH_x$/Pt(111) under UHV and a CO atmosphere. (a−c) Configurations of $MnOH_x$/Pt(111) interface structures within the experimental preparation condition (5×10^{-7} mbar H_2 and 298 K) and the reaction condition (UHV vs 5×10^{-7} mbar CO): (a) 89% H-covered $Mn_9O_9H_8$/Pt, (b) OH-saturated (at Mn edge) $Mn_9O_{10}H_9$/Pt, and (c) CO-saturated $Mn_9O_{10}H_9$/Pt ribbons. H: white; C: black; O: red; Mn: light violet; Pt: dark blue. (d and e) Ab initio thermodynamic phase diagrams for the hydroxylation degree and CO saturation on $MnOH_x$/Pt: (d) H coverage on the Mn_9O_9/Pt ribbon, (e) OH saturation on $Mn_9O_9H_8$/Pt, and (f) CO saturation at the perimeter of (b). (g) Free energy diagram for H_2O generation from two OH* at the perimeters (Mn edge and O edge) of (b) at 453 K. (h) Free energy diagrams for the CO + 2OH → $CO_2 + H_2O$ process at 363 K (the first stage, starting from (c)) and the CO + 2OH → $CO_2 + H_2 + O_L$ process at 403 K (the second stage) via the COOH* intermediate. Inserted numbers denote the barriers of elementary steps.

CO is low because CO starts to react with OD at 363 K. The consumption of OD content is larger in CO from 403 to 483 K (34%) compared with that under UHV (30%), which also suggests that CO does participate in the reaction in this temperature range. Hence, it is proposed that the main reaction between CO and OD from 403 to 483 K is:

$$CO + 2OD \rightarrow CO_2 + D_2 + O_L\ (50\% \le OD \le 85\%) \quad (4)$$

After annealing to higher temperature in CO, OD content keeps on decreasing, whereas O_L content remains almost unchanged. When annealing to 543 K in CO, OD content decreases to 26%, and O_L content remains stable. This result is similar to reaction 3, while the surface is highly reduced after annealing to 543 K in CO in contrast to the surface where reaction 3 occurs. It is more reasonable that reaction 4 still proceeds and CO begins to react with O_L in this temperature range. Therefore, the main reaction between surface OD and O_L from 483 to 543 K should be:

$$CO + 2OD \rightarrow CO_2 + D_2 + O_L \text{ and } CO + O_L \rightarrow CO_2$$

as well as

$$2CO + 2OD \rightarrow 2CO_2 + D_2\ (26\% \le OD \le 50\%) \quad (5)$$

Figure S6 presents D_2 and CO_2 mass spectra of $MnOD_x$ and Mn_3O_4 films during annealing in CO from room temperature to 748 K, respectively. There are two sharp D_2 signal peaks located at 56 and 77 s corresponding to around 466 and 529 K when annealing $MnOD_x$ in CO, which indicates the occurrence of reactions (4) and (5). In Figure S6b, there are

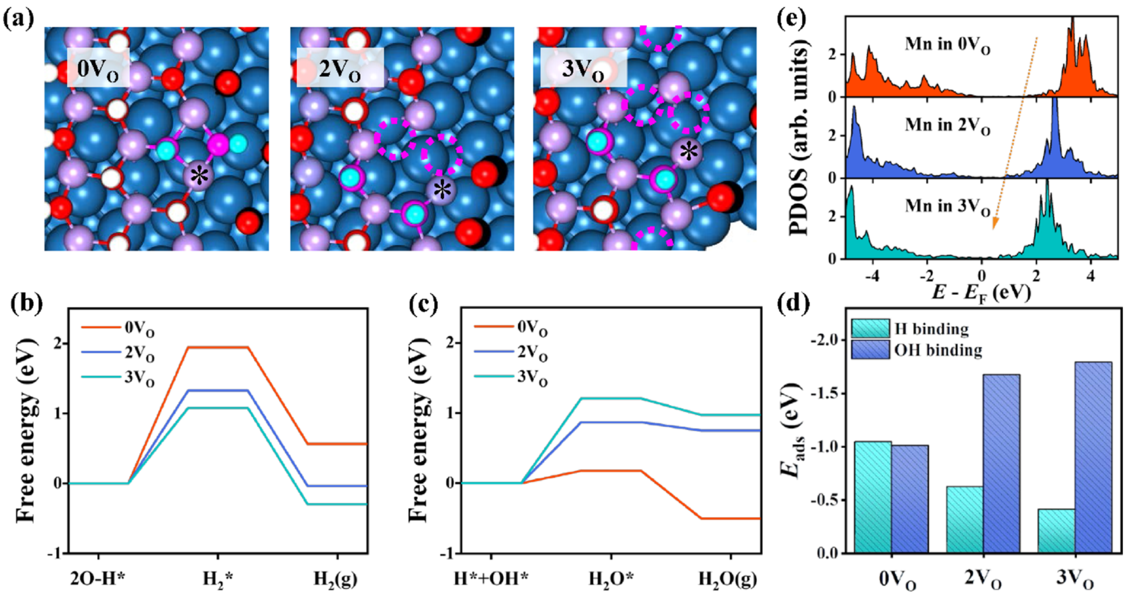

Figure 6. Nature of difference of OH evolution into H_2O vs H_2. (a) Configurations of $MnOH_x/Pt(111)$ interface structures with various V_O contents ($0V_O$ denotes no O vacancy and $2V_O$ denotes two O vacancies). H: white and cyan; C: black; O: red and pink; Mn: light violet; Pt: dark blue. O vacancies: dashed pink circle. (b and c) Free energy diagrams of OH* evolution into H_2O vs H_2 processes as OH content decreases (i.e., V_O increases). (d) Tendency of H vs OH binding on $MnOH_x/Pt(111)$ as OH content decreases. (e) Projected density of states of the Mn (3*d*) sites (denoted by black stars in a) in the three models. The orange arrow shows the trend of the unoccupied states of Mn 3*d* orbitals downshifting toward the Fermi level.

two CO_2 mass signal peaks located at 50 and 75 s that are very close to the D_2 peak position in Figure S6a when annealing $MnOD_x$ in CO. Compared with the $MnOD_x$ film, no D_2 mass signal peak emerges during the CO annealing process. A sharp CO_2 peak located at 75 s emerges when annealing the Mn_3O_4 film in CO, indicating the occurrence of reaction 1.

Evolution Mechanism of Surface OH under UHV and a CO Atmosphere. DFT calculations are carried out to gain insights into the mechanism of OH evolution on $MnOH_x/Pt(111)$. Two questions will be addressed: (1) how does CO promote H_2O generation compared to UHV annealing? and (2) what is the reason for product transformation from H_2O to H_2 as OH coverage decreases? According to STM results, we adopt an MnO-(3 × 3)/Pt(111)-($\sqrt{13} \times \sqrt{13}$) moiré structure[36] and then generate the hydroxylated structures to simulate the hexagonal $MnOH_x$ on Pt(111) (Figures S7 and S5). Through the ab initio thermodynamic phase diagram, we find that saturation of H coverage is 78% on the $Mn_9O_9/Pt(111)$ film (Figure S7a) and 89% for $Mn_9O_9/Pt(111)$ ribbon (Figure 5a) under 5×10^{-7} mbar H_2 at room temperature. Figure 5b,e shows that the Mn edge of $Mn_9O_9H_8/Pt(111)$ ribbon can be saturated by extra one bridging OH* to form an $Mn_9O_{10}H_9/Pt(111)$ ribbon, whereas OH* at both Mn and O edges cannot be removed at room temperature. We thus infer that the initial hydroxylated $MnOD_x/Pt(111)$ sample with 94% OD content features an abundant D-covered surface and a slight OD-saturated perimeter (at Mn edge) as $Mn_9O_{10}H_9/Pt(111)$ ribbon described. Figure 5f shows that the two edges of $Mn_9O_{10}H_9/Pt(111)$ ribbon can be saturated by CO adsorption under 5×10^{-7} mbar CO until ~500 K, and thus the ribbon with CO saturation can represent the initial hydroxylation structure under a CO atmosphere (e.g., the model in Figure 5c).

For OH evolution under UHV, on the surface of the $Mn_9O_9H_7/Pt(111)$ film (Figure S7) the barrier (termed G_a) for H_2 generation is 2.62 eV limited by the O−H* to Mn−H* diffusion, and that for H_2O generation should exceed 1.64 eV estimated by the reaction energy from OH* to H_2O*. Such high barriers imply that the film surface is not reactive at 453 K. At the perimeter of the $Mn_9O_{10}H_9/Pt(111)$ ribbon, the reaction energies from OH* to H_2* are 1.93 eV at the Mn edge and 2.87 eV at the O edge, respectively, indicating an impossibility of H_2 generation (Figure S8). In contrast, H_2O generation is feasible to occur at the Mn edge with a low barrier (G_a = 0.91 eV) rather than at the O edge with an insurmountable barrier (G_a = 2.07 eV) (Figures 5g, S9a and S9b). This well explains the experimental observation in Figure 3 that the OH reaction leads to the generation of H_2O at the Mn edge of the submonolayer $MnOH_x/Pt(111)$.

As for OH evolution in the CO atmosphere, three possible mechanisms are proposed including CO modification, V_O promotion, and COOH* mediation. (i) As shown in Figures S10, 5h, and S11a, if the perimeter is modified by CO adsorption, the direct H_2O generation from OH* would possess a 1.06 eV barrier, which is slightly higher than that without CO adsorption (G_a = 0.91 eV) (Figure S10a,b). This implies no promotion effect on H_2O generation through CO modification. (ii) If O_L at the perimeter was preferentially removed by CO (G_a = 0.75 eV), the subsequent H_2O generation would overcome a 1.05 eV barrier (Figures S10c,d), indicating that V_O does not boost H_2O generation neither. (iii) If OH at the perimeter reacted with CO to form the COOH* intermediate (Figures 5h and S11a) which is found to be barrierless through CO inserting the Mn−OH bond, G_a for next H_2O generation from COOH* would be lowered to 0.42 eV, indicating a promotion effect via COOH* mediation. Then, CO can consume the remaining O_L to form CO_2 by surmounting a 0.78 eV barrier. We also note that COOH* can stem from CO* on Pt reacting with interfacial OH* as reported,[37] which is excluded because of the strong CO−Pt bonding leading to a high barrier (G_a = 0.99 eV). Therefore, we suggest that OH* reacting with CO to form COOH* intermediate promotes H_2O generation under a CO atmosphere, which accounts for that the reaction of CO + 2OH → CO_2 + H_2O occurs via a COOH*-mediated mechanism when annealing the $MnOH_x$/Pt sample from 363 to 403 K.

Starting from the interface with two OH lost (termed $2V_O$), Figures 5h and S11b show a possible pathway toward H_2 generation, including CO adsorption, CO* reacting with OH* to form COOH* (G_a = 1.29 eV, TS2), O−H* in COOH* diffusing to Mn−H* (G_a = 0.43 eV, TS3), CO_2* desorption, H_2* generation (G_a = 1.55 eV, TS5) through reverse H_2 heterolysis, and H_2* desorption with one O_L left. Notably, the direct O−H* to Mn−H* diffusion needs to overcome a barrier of >2 eV which is hindered at 403 K. On the contrary, formation of the COOH* intermediate promotes O−H* diffusion to Mn−H*, which plays a crucial role in H_2 generation. In addition, we investigate the reverse H spillover from the $MnOH_x$ overlayer to Pt substrate as shown in Figure S12. The bridged O−H* at both O and Mn edges is more stable by at least 0.9 eV than Pt−H*, and the reverse spillover barrier is about 1.5 eV. The triple O−H* at the Mn edge is hard to diffuse to Pt−H* with a 2.35 eV barrier though they are of similar stability. We thus determine that OH* preferentially reacts with CO to form a COOH* intermediate and then to generate H_2 instead of reversely diffusing to form Pt−H*, that is, CO + 2OH → CO_2 + H_2 + O_L (the second stage at 403−483 K).

We further try to understand the origin of product selectivity (H_2O vs H_2) as OH content decreases. Based on the three models in Figure 6a, that is, from the pristine ($0V_O$), the two OH-removing ($2V_O$), to the three OH-removing ($3V_O$) interfaces, we find that H_2 generation is gradually exothermic (Figure 6b) as θ_{OH} decreases but the trend for H_2O generation is opposite (Figure 6c). Through quantifying the H and OH bindings (E_{ads}, see the SI for the formulae), we find that OH binding is strengthened, but H binding is weakened (Figure 6d) as θ_{OH} decreases, which just corresponds to the easy H_2 generation but hard H_2O generation. Indeed, H/OH binding strength is tightly related to the electronic characters of their adjacent Mn sites. As shown in Figure 6e, the decrease of θ_{OH} induces a downshift of the unoccupied states of Mn 3*d* toward the Fermi level, indicative of a reduction of Mn. Therefore, we suggest that the decrement of the θ_{OH} promotes the reduction of Mn which in turn tunes H binding toward a weakened strength while OH binding toward the opposite direction.

Scheme 1 illustrates the reaction of CO with the $MnOH_x$ surface in different temperature ranges. Experiments and DFT calculations clarify that the reaction pathway can be modulated by θ_{OH} and V_O density. When annealing the $MnOH_x$ film between 363 and 403 K in CO, OH coverage decreases by 9% and O_L content remains almost unchanged. DFT calculations reveal that interfacial OH reacts with CO to generate H_2O via the COOH* intermediate with a low energy barrier than annealing under UHV. Therefore, the main reaction product should be H_2O in this temperature range. When annealing the $MnOH_x$ film between 403 and 483 K in CO, θ_{OH} decreases by 34% and O_L content increases by 17%. As θ_{OH} decreases and V_O density increases, DFT calculations suggest a weakened trend for H binding and an enhanced trend for OH, implying the tendency for H_2 production and the suppression for H_2O formation. Thus, the main reaction product should be H_2 and O_L in this temperature window. When annealing the $MnOH_x$ film between 483 and 543 K in CO, O_L content remains stable and θ_{OH} decreases by 24.8%. It is considered that CO still reacts with OH to produce H_2 and O_L, and CO also reacts with O_L to produce CO_2.

Scheme 1. Reaction on the $MnOH_x$/Pt(111) Surface When Annealing in CO to Different Temperatures

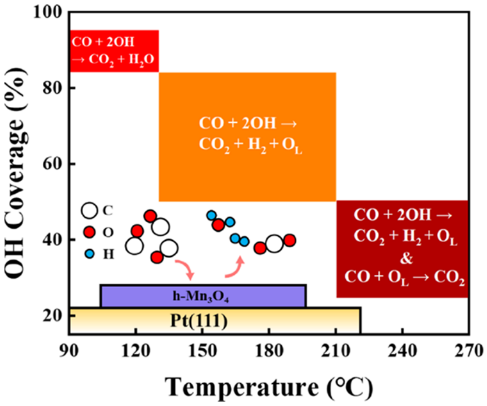

■ CONCLUSIONS

The hydroxylation process of Mn_3O_4/Pt(111) by D_2 at room temperature is investigated by XPS and STM, and an $MnOH_x$ film with 94% OH coverage can be obtained. Surface science experiments and DFT calculations are combined to elaborate the evolution of surface OH under UHV and a CO atmosphere. It is found that OH mainly desorbs in the form of H_2O when annealing under UHV. While under a CO atmosphere, our results indicate that the reaction type is adjusted by surface θ_{OH} and V_O density, which can be divided into three stages. With OH coverage from 94 to 85%, interfacial OH reacts with CO to produce H_2O and CO_2 (363 K ≤ T ≤ 403 K). With θ_{OH} from 85 to 50%, in addition to the formation of CO_2, it is inclined to generate H_2 and O_L instead of H_2O, which is due to the weakened H binding and enhanced OH binding on interfacial Mn sites (403 K ≤ T ≤ 483 K). With θ_{OH} from 50 to 26%, apart from the reaction occurring at the last stage, CO also reacts with O_L to form CO_2 (483 K ≤ T ≤ 543 K). This work not only provides a detailed understanding of the surface structure−performance relationship in the CO conversion reaction over $MnOH_x$/Pt, but also renders guidance for the rational design of catalysts for WGS and PROX reactions. We also expect that the established relationship between reaction selectivity and defect contents can be widely applied in other oxide catalytic systems.

■ ASSOCIATED CONTENT

Supporting Information

The Supporting Information is available free of charge at https://pubs.acs.org/doi/10.1021/acscatal.2c03337.

Experimental method, computational details, model constructions, additional discussion, figures, and table (PDF)

■ AUTHOR INFORMATION

Corresponding Authors

Rentao Mu − *State Key Laboratory of Catalysis, Dalian Institute of Chemical Physics, Chinese Academy of Sciences,* *Dalian 116023, China;* orcid.org/0000-0002-2872-0152; Email: murt@dicp.ac.cn

Qiang Fu − *Zhang Dayu School of Chemistry, Dalian University of Technology, Dalian 116024, China; State Key Laboratory of Catalysis, Dalian Institute of Chemical Physics, Chinese Academy of Sciences, Dalian 116023, China;* orcid.org/0000-0001-5316-6758; Email: qfu@dicp.ac.cn

Authors

Rankun Zhang − *Zhang Dayu School of Chemistry, Dalian University of Technology, Dalian 116024, China; State Key Laboratory of Catalysis, Dalian Institute of Chemical Physics, Chinese Academy of Sciences, Dalian 116023, China*

Le Lin − *State Key Laboratory of Catalysis, Dalian Institute of Chemical Physics, Chinese Academy of Sciences, Dalian 116023, China*

Dongqing Wang − *State Key Laboratory of Catalysis, Dalian Institute of Chemical Physics, Chinese Academy of Sciences, Dalian 116023, China; University of Chinese Academy of Sciences, Beijing 100039, China*

Yijing Liu − *State Key Laboratory of Catalysis, Dalian Institute of Chemical Physics, Chinese Academy of Sciences, Dalian 116023, China; University of Chinese Academy of Sciences, Beijing 100039, China*

Yunjian Ling − *State Key Laboratory of Catalysis, Dalian Institute of Chemical Physics, Chinese Academy of Sciences, Dalian 116023, China; University of Chinese Academy of Sciences, Beijing 100039, China*

Siqin Zhao − *State Key Laboratory of Catalysis, Dalian Institute of Chemical Physics, Chinese Academy of Sciences, Dalian 116023, China; University of Chinese Academy of Sciences, Beijing 100039, China*

Complete contact information is available at: https://pubs.acs.org/10.1021/acscatal.2c03337

Author Contributions

[#]R.Z. and L.L. contributed equally to this work

Notes

The authors declare no competing financial interest.

■ ACKNOWLEDGMENTS

This work was financially supported by the National Key R&D Program of China (2021YFA1502800), the National Natural Science Foundation of China (Nos. 91945302, 21825203, and 22288201), Photon Science Center for Carbon Neutrality, LiaoNing Revitalization Talents Program (XLYC1902117), and the Dalian National Laboratory for Clean Energy (DNL) Cooperation Fund (DNL201907).

■ REFERENCES

(1) Graciani, J.; Mudiyanselage, K.; Xu, F.; Baber Ashleigh, E.; Evans, J.; Senanayake Sanjaya, D.; Stacchiola Darío, J.; Liu, P.; Hrbek, J.; Sanz, J. F.; Rodriguez, J. A. Highly Active Copper-Ceria and Copper-Ceria-Titania Catalysts for Methanol Synthesis from CO_2. *Science* **2014**, *345*, 546−550.

(2) Kattel, S.; Ramírez Pedro, J.; Chen Jingguang, G.; Rodriguez José, A.; Liu, P. Active Sites for CO_2 Hydrogenation to Methanol on Cu/ZnO Catalysts. *Science* **2017**, *355*, 1296−1299.

(3) Wang, J.; Zhang, G.; Zhu, J.; Zhang, X.; Ding, F.; Zhang, A.; Guo, X.; Song, C. CO_2 Hydrogenation to Methanol over In_2O_3-Based Catalysts: From Mechanism to Catalyst Development. *ACS Catal.* **2021**, *11*, 1406−1423.

(4) Ye, T.-N.; Park, S.-W.; Lu, Y.; Li, J.; Sasase, M.; Kitano, M.; Tada, T.; Hosono, H. Vacancy-Enabled N_2 Activation for Ammonia Synthesis on an Ni-Loaded Catalyst. *Nature* **2020**, *583*, 391−395.

(5) Marnellos, G.; Stoukides, M. Ammonia Synthesis at Atmospheric Pressure. *Science* **1998**, *282*, 98−100.

(6) Jiao, K.; Xuan, J.; Du, Q.; Bao, Z.; Xie, B.; Wang, B.; Zhao, Y.; Fan, L.; Wang, H.; Hou, Z.; Huo, S.; Brandon, N. P.; Yin, Y.; Guiver, M. D. Designing the Next Generation of Proton-Exchange Membrane Fuel Cells. *Nature* **2021**, *595*, 361−369.

(7) Wang, X. X.; Swihart, M. T.; Wu, G. Achievements, Challenges and Perspectives on Cathode Catalysts in Proton Exchange Membrane Fuel Cells for Transportation. *Nat. Catal.* **2019**, *2*, 578−589.

(8) Yang, Y.; Dai, Q.; Shi, L.; Liu, Y.; Isimjan, T. T.; Yang, X. Electronic Modulation of Pt Nanoparticles on Ni_3N-Mo_2C by Support-Induced Strategy for Accelerating Hydrogen Oxidation and Evolution. *J. Phys. Chem. Lett.* **2022**, *13*, 2107−2116.

(9) Rodriguez, J. A.; Ma, S.; Liu, P.; Hrbek, J.; Evans, J.; Pérez, M. Activity of CeO_x and TiO_x Nanoparticles Grown on Au(111) in the Water-Gas Shift Reaction. *Science* **2007**, *318*, 1757−1760.

(10) Zhang, Z.; Chen, X.; Kang, J.; Yu, Z.; Tian, J.; Gong, Z.; Jia, A.; You, R.; Qian, K.; He, S.; Teng, B.; Cui, Y.; Wang, Y.; Zhang, W.; Huang, W. The Active Sites of Cu-ZnO Catalysts for Water Gas Shift and CO Hydrogenation Reactions. *Nat. Commun.* **2021**, *12*, 4331.

(11) Fu, Q.; Saltsburg, H.; Flytzani-Stephanopoulos, M. Active Nonmetallic Au and Pt Species on Ceria-Based Water-Gas Shift Catalysts. *Science* **2003**, *301*, 935−938.

(12) Chen, G.; Zhao, Y.; Fu, G.; Duchesne Paul, N.; Gu, L.; Zheng, Y.; Weng, X.; Chen, M.; Zhang, P.; Pao, C.-W.; Lee, J.-F.; Zheng, N. Interfacial Effects in Iron-Nickel Hydroxide-Platinum Nanoparticles Enhance Catalytic Oxidation. *Science* **2014**, *344*, 495−499.

(13) Cao, L.; Liu, W.; Luo, Q.; Yin, R.; Wang, B.; Weissenrieder, J.; Soldemo, M.; Yan, H.; Lin, Y.; Sun, Z.; et al. Atomically Dispersed Iron Hydroxide Anchored on Pt for Preferential Oxidation of CO in H_2. *Nature* **2019**, *565*, 631−635.

(14) Ayastuy, J. L.; González-Marcos, M. P.; González-Velasco, J. R.; Gutiérrez-Ortiz, M. A. $MnO_x/Pt/Al_2O_3$ Catalysts for CO Oxidation in H_2-Rich Streams. *Appl. Catal., B* **2007**, *70*, 532−541.

(15) Kalamaras, C. M.; Americanou, S.; Efstathiou, A. M. "Redox" vs "Associative Formate with -OH Group Regeneration" WGS Reaction Mechanism on Pt/CeO_2: Effect of Platinum Particle Size. *J. Catal.* **2011**, *279*, 287−300.

(16) Zhang, Z.-S.; Fu, Q.; Xu, K.; Wang, W.-W.; Fu, X.-P.; Zheng, X.-S.; Wu, K.; Ma, C.; Si, R.; Jia, C.-J.; Sun, L.-D.; Yan, C.-H. Intrinsically Active Surface in a Pt/γ-Mo_2N Catalyst for the Water-Gas Shift Reaction: Molybdenum Nitride or Molybdenum Oxide? *J. Am. Chem. Soc.* **2020**, *142*, 13362−13371.

(17) Rodriguez, J. A.; Ramírez, P. J.; Asara, G. G.; Viñes, F.; Evans, J.; Liu, P.; Ricart, J. M.; Illas, F. Charge Polarization at a Au−TiC Interface and the Generation of Highly Active and Selective Catalysts for the Low-Temperature Water-Gas Shift Reaction. *Angew. Chem., Int. Ed.* **2014**, *53*, 11270−11274.

(18) Xu, M.; Yao, S.; Rao, D.; Niu, Y.; Liu, N.; Peng, M.; Zhai, P.; Man, Y.; Zheng, L.; Wang, B.; Zhang, B.; Ma, D.; Wei, M. Insights into Interfacial Synergistic Catalysis over $Ni@TiO_{2-x}$ Catalyst toward Water-Gas Shift Reaction. *J. Am. Chem. Soc.* **2018**, *140*, 11241−11251.

(19) Fu, X.-P.; Guo, L.-W.; Wang, W.-W.; Ma, C.; Jia, C.-J.; Wu, K.; Si, R.; Sun, L.-D.; Yan, C.-H. Direct Identification of Active Surface Species for the Water-Gas Shift Reaction on a Gold-Ceria Catalyst. *J. Am. Chem. Soc.* **2019**, *141*, 4613−4623.

(20) Li, Y.; Kottwitz, M.; Vincent, J. L.; Enright, M. J.; Liu, Z.; Zhang, L.; Huang, J.; Senanayake, S. D.; Yang, W.-C. D.; Crozier, P. A.; et al. Dynamic Structure of Active Sites in Ceria-Supported Pt Catalysts for the Water Gas Shift Reaction. *Nat. Commun.* **2021**, *12*, 914.

(21) Davó-Quiñonero, A.; Navlani-García, M.; Lozano-Castelló, D.; Bueno-López, A.; Anderson, J. A. Role of Hydroxyl Groups in the

Preferential Oxidation of CO over Copper Oxide-Cerium Oxide Catalysts. *ACS Catal.* **2016**, *6*, 1723−1731.

(22) Tanaka, K.-I.; Shou, M.; He, H.; Shi, X.; Zhang, X. Dynamic Characterization of the Intermediates for Low-Temperature PROX Reaction of CO in H_2—Oxidation of CO with OH via HCOO Intermediate. *J. Phys. Chem. C* **2009**, *113*, 12427−12433.

(23) Ribeiro, M. C.; Jacobs, G.; Graham, U. M.; Azzam, K. G.; Linganiso, L.; Davis, B. H. Low Temperature Water-Gas Shift: Differences in Oxidation States Observed with Partially Reduced Pt/MnO_X and Pt/CeO_X Catalysts Yield Differences in OH Group Reactivity. *Catal. Commun.* **2010**, *11*, 1193−1199.

(24) Nie, L.; Mei, D.; Xiong, H.; Peng, B.; Ren, Z.; Hernandez, X. I. P.; Delariva, A.; Wang, M.; Engelhard, M. H.; Kovarik, L.; Datye, A. K.; Wang, Y. Activation of Surface Lattice Oxygen in Single-Atom Pt/CeO_2 for Low-Temperature CO Oxidation. *Science* **2017**, *358*, 1419−1423.

(25) Xu, L.; Zhang, W.; Zhang, Y.; Wu, Z.; Chen, B.; Jiang, Z.; Ma, Y.; Yang, J.; Huang, W. Oxygen Vacancy-Controlled Reactivity of Hydroxyls on an FeO(111) Monolayer Film. *J. Phys. Chem. C* **2011**, *115*, 6815−6824.

(26) Chen, B.; Ma, Y.; Ding, L.; Xu, L.; Wu, Z.; Yuan, Q.; Huang, W. Reactivity of Hydroxyls and Water on a CeO_2(111) Thin Film Surface: The Role of Oxygen Vacancy. *J. Phys. Chem. C* **2013**, *117*, 5800−5810.

(27) Hagendorf, C.; Sachert, S.; Bochmann, B.; Kostov, K.; Widdra, W. Growth, Atomic Structure, and Vibrational Properties of MnO Ultrathin Films on Pt(111). *Phys. Rev. B* **2008**, *77*, No. 075406.

(28) Langell, M. A.; Hutchings, C. W.; Carson, G. A.; Nassir, M. H. High Resolution Electron Energy Loss Spectroscopy of MnO(100) and Oxidized MnO(100). *J. Vac. Sci. Technol., A* **1996**, *14*, 1656−1661.

(29) Kundu, A. K.; Menon, K. S. R. Growth and Characterization of Ultrathin Epitaxial MnO film on Ag(001). *J. Cryst. Growth* **2016**, *446*, 85−91.

(30) Zhang, L.; Tang, Z.; Wang, S.; Ding, D.; Chen, M.; Wan, H. Growth and Vibrational Properties of MnO_x Thin Films on Rh(111). *Surf. Sci.* **2012**, *606*, 1507−1511.

(31) Li, Y.; Lin, L.; Mu, R.; Liu, Y.; Zhang, R.; Wang, C.; Ning, Y.; Fu, Q.; Bao, X. Activation of CO over Ultrathin Manganese Oxide Layers Grown on Au(111). *ACS Catal.* **2021**, *11*, 849−857.

(32) Zhao, S.; Lin, L.; Huang, W.; Zhang, R.; Wang, D.; Mu, R.; Fu, Q.; Bao, X. Design of Lewis Pairs via Interface Engineering of Oxide-Metal Composite Catalyst for Water Activation. *J. Phys. Chem. Lett.* **2021**, *12*, 1443−1452.

(33) Merte, L. R.; Knudsen, J.; Grabow, L. C.; Vang, R. T.; Lægsgaard, E.; Mavrikakis, M.; Besenbacher, F. Correlating STM Contrast and Atomic-Scale Structure by Chemical Modification: Vacancy Dislocation Loops on FeO/Pt(111). *Surf. Sci.* **2009**, *603*, L15−L18.

(34) Knudsen, J.; Merte, L. R.; Grabow, L. C.; Eichhorn, F. M.; Porsgaard, S.; Zeuthen, H.; Vang, R. T.; Lægsgaard, E.; Mavrikakis, M.; Besenbacher, F. Reduction of FeO/Pt(111) Thin Films by Exposure to Atomic Hydrogen. *Surf. Sci.* **2010**, *604*, 11−20.

(35) Norton, P. R.; Goodale, J. W.; Selkirk, E. B. Adsorption of CO on Pt(111) Studied by Photoemission, Thermal Desorption Spectroscopy and High Resolution Dynamic Measurements of Work Function. *Surf. Sci.* **1979**, *83*, 189−227.

(36) Zeng, Z.; Chang, K.-C.; Kubal, J.; Markovic, N. M.; Greeley, J. Stabilization of Ultrathin (Hydroxy)oxide Films on Transition Metal Substrates for Electrochemical Energy Conversion. *Nat. Energy* **2017**, *2*, 17070.

(37) Gu, X.-K.; Ouyang, R.; Sun, D.; Su, H.-Y.; Li, W.-X. CO Oxidation at the Perimeters of an FeO/Pt(111) Interface and How Water Promotes the Activity: A First-Principles Study. *ChemSusChem* **2012**, *5*, 871−878.